Article

Time-Dependent Density Matrix Renormalization Group Method for Quantum Transport with Phonon Coupling in Molecular Junction

Hengrui Yang, Weitang Li, Jiajun Ren, and Zhigang Shuai*

Cite This: *J. Chem. Theory Comput.* 2023, 19, 6070−6081

Read Online

ACCESS | Metrics & More | Article Recommendations | Supporting Information

ABSTRACT: Quantum transport in molecular junctions has attracted great attention. The charge motion in a molecular junction can cause geometric deformation, leading to strong electron phonon coupling, which was often overlooked. We have formulated a nearly exact method to assess the time-dependent current and occupation number in the molecular junction modeled by the electron−phonon coupled bridge state using the time-dependent density matrix renormalization group (TD-DMRG) method. The oscillation period and amplitude of the current are found to be dependent on the electron phonon coupling strength and energy level alignment with the electrodes. In an attempt to better understand these phenomena, we have devised a new approximation that explains the bistability phenomenon and the behavior of steady currents in the strong electron−phonon coupling regime. Comparisons have been made with the multilayer-multiconfiguration time-dependent Hartree (ML-MCTDH) method and the analytical result in the purely electronic limit. Furthermore, we explore the entropy of different orderings, extending to the electron phonon model problems. Regarding finite temperature, the thermal Bogoliubov transformation of both fermions and bosons is used and compared with imaginary time evolution results.

$$I_\xi(t) = \pm \frac{dN_\xi(t)}{dt} = \pm \frac{1}{tr[\rho]} tr\{\rho e^{iHt} i[H, N_\xi] e^{-iHt}\}$$
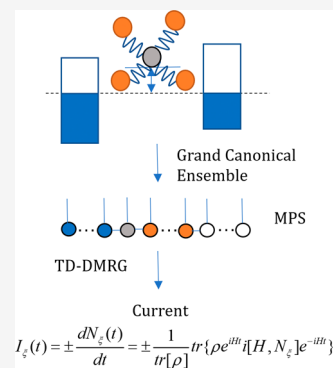
1. INTRODUCTION

The quantum transport in molecular junctions has seen great progress in recent years.[1−5] Single molecular junction has been widely used to study nonequilibrium many-body quantum phenomena on the nanoscale. Application has been demonstrated successfully in molecular electronics/molecular devices[3−7] and scanning tunneling microscopy (STM).[1,3−5,7−9] Interesting phenomena have emerged such as Coulomb blockade,[10] Kondo effect,[8] chiral-induced spin selectivity,[11,12] phonon blockade,[13] hysteresis,[9] etc.

The charge occupation number at the molecular bridge site often changes with the molecular geometry. In fact, vibrational contributions have been observed in the experimental measurement of currents or current−voltage curves.[14] By and large, organic molecules are flexible, naturally leading to large vibrational coupling.[15]

A number of theoretical methods have been developed to tackle those problems of quantum transport in molecular junctions with interactions, such as nonequilibrium Green function (NEGF) methods,[16−18] scattering theory,[19] and master equation methods.[20,21] NEGF and master equation approaches usually rely on perturbation treatments. We intend to develop a nearly exact, robust, and systematic numerical method to study quantum transport problems with consideration of many-body effects.

Numerical methods have been developed to achieve this goal, such as quantum Monte Carlo,[22] dynamical mean-field theory (DMFT),[23] numerical renormalization group,[24] hierarchical equations of motion (HEOM),[25] and the multilayer multiconfiguration time-dependent Hartree (ML-MCTDH)[10,13] method. In this paper, we propose to use the time-dependent density matrix renormalization group (TD-DMRG) method, in close comparison with ML-MCTDH.

DMRG is a specific structure of a tensor network[26] which is nearly exact for one-dimensional quantum many particle systems. It was established by White in 1992.[27,28] Since then, many new algorithms have been developed, such as dynamical DMRG,[29] finite temperature,[30] and time-evolving methods.[31−33] Recently, we have implemented the GPU acceleration algorithms[34] and proposed a general automatic construction method for the matrix product operators.[35] We further presented a general picture for carrier transport in organic semiconductors combining DMRG and the Kubo formula with the Holstein−Peierls model[36,37] featuring both inter- and intramolecular vibrational couplings and applied its algorithm to calculate the thermoelectric power factor.[38] There have been theoretical works to calculate electron transport of molecular junction using DMRG[23,39−45] without considering the electron phonon interactions. In this work, we develop an algorithm to study a general model of vibrationally coupled electron transport in molecular junctions, based on time-dependent DMRG, at both zero and finite temperature.

2. THEORETICAL MODEL AND METHODOLOGICAL APPROACH

2.1. Model Hamiltonian. The vibrationally coupled electron transport model in the molecule junction has been proposed previously.[13] The simplest model consists of a single molecular site, harmonic oscillators coupled to the molecule, and the left and right leads. The Hamiltonian reads:

$$H = H_{el} + H_{nuc} + H_{el-nuc} \tag{1}$$

$$H_{el} = E_d d^+ d + \sum_{k_L} E_{k_L} c_{k_L}^+ c_{k_L} + \sum_{k_R} E_{k_R} c_{k_R}^+ c_{k_R}$$
$$+ \sum_{k_L} V_{dk_L} (c_{k_L}^+ d + d^+ c_{k_L}) + \sum_{k_R} V_{dk_R} (c_{k_R}^+ d + d^+ c_{k_R}) \tag{2}$$

$$H_{nuc} = \frac{1}{2} \sum_j (P_j^2 + \omega_j^2 Q_j^2) = \sum_j \omega_j \left(a_j^+ a_j + \frac{1}{2} \right) \tag{3}$$

$$H_{el-nuc} = d^+ d \sum_j c_j Q_j = d^+ d \sum_j \frac{c_j}{\sqrt{2\omega_j}} (a_j^+ + a_j) \tag{4}$$

which describes pure electronic terms of the system and leads, vibration of the system, and electron vibration couplings, respectively. The bath Hamiltonian is diagonal; namely, there is no coupling between bath sites. d^+ (d) is the electron creation (annihilation) operator of the molecular bridge. c's are from the left and right leads, respectively. a_j^+ and a_j are phonon creation and annihilation operators, while P_j/Q_j are the momentum and displacement operators of normal modes. E_d is the onsite energy of the molecular bridge, and E_{k_L} and E_{k_R} are the onsite energies of the left and right electrodes, respectively. V_{dk_L}, and V_{dk_R} are coupling strengths between the molecular bridge and leads. These are calculated by the following width functions and the corresponding continuous functions:

$$\begin{cases} \Gamma_L(E) = 2\pi \sum_{k_L} |V_{dk_L}|^2 \delta(E - E_{k_L}) \\ \Gamma_R(E) = 2\pi \sum_{k_R} |V_{dk_R}|^2 \delta(E - E_{k_R}) \end{cases} \tag{5}$$

$$\Gamma(E) = \begin{cases} \dfrac{\alpha_e^2}{\beta_e^2} \sqrt{4\beta_e^2 - E^2} & |E| \leq 2|\beta_e| \\ 0 & |E| \geq 2|\beta_e| \end{cases} \tag{6}$$

$$\begin{cases} \Gamma_L(E) = \Gamma(E - \mu_L) \\ \Gamma_R(E) = \Gamma(E - \mu_R) \end{cases} \tag{7}$$

The applied bias voltage changes the chemical potentials of left and right leads with a Fermi surface at 0 eV.

$$\mu_{L/R} = \pm V/2 \tag{8}$$

The electronic continua are discretized evenly, i.e., with equal separation in the interval $[-2\beta_e, 2\beta_e]$, though different schemes had been tried.[45] ω_j is the frequency of normal nodes. c_j is the electron−nuclear coupling constant, or $c_j/(\omega_j\sqrt{2\omega_j})$ is the dimensionless electron−phonon coupling constant. These can be calculated by the following spectral density function and the

corresponding continuous functions is the Ohmic spectral density function:

$$J(\omega) = \frac{\pi}{2} \sum_j \frac{c_j^2}{\omega_j} \delta(\omega - \omega_j) \tag{9}$$

$$J_O(\omega) = \frac{\pi}{2} \alpha \omega e^{-\omega/\omega_c} \tag{10}$$

The discretization is different from that of the fermion bath, which is not evenly distributed, and ω_j and c_j can be acquired from the integral of $\rho(\omega)$:

$$\rho(\omega) = \frac{N+1}{\omega_c} e^{-\omega/\omega_c} \tag{11}$$

$$\int_0^{\omega_j} d\omega \, \rho(\omega) = j, \quad j = 1, 2, ..., N \tag{12}$$

$$\omega_j = -\omega_c \ln\left(1 - \frac{j}{N+1}\right) \tag{13}$$

$$c_j = \sqrt{\frac{2}{\pi} \omega_j \frac{J_O(\omega_j)}{\rho(\omega_j)}} = \sqrt{\frac{\alpha \omega_j^2 \omega_c}{N+1}} \tag{14}$$

Due to the role of leads or chemical potential, a grand canonical ensemble should be considered. At finite temperature, the initial density matrix is

$$\rho = \rho_d^0 \, e^{-\beta(H_0 - \mu_L N_L - \mu_R N_R)} \tag{15}$$

in which

$$H_0 = \sum_{k_L} E_{k_L} c_{k_L}^+ c_{k_L} + \sum_{k_R} E_{k_R} c_{k_R}^+ c_{k_R} + H_{nuc}^0 \tag{16}$$

and ρ_d^0 is the initial density matrix of the molecular bridge. $N_\xi = \sum_{k_\xi} c_{k_\xi}^+ c_{k_\xi}(\xi = L, R)$ represents the occupation number in each lead. Eq 15 represents a grand canonical ensemble description. H_{nuc}^0 is the equilibrium initial phonon bath Hamiltonian. It equals H_{nuc} if the bridge state is unoccupied initially, and it becomes $H_{nuc} + \sum_j c_j Q_j$ if the bridge state is occupied initially, namely, a displaced harmonic oscillator. The nonequilibrium initial phonon bath has been discussed in the literature.[46,47] At zero temperature, the density matrix becomes a pure state, which should be the ground state of $H_0 - \mu_L N_L - \mu_R N_R$.

With the time-evolving Hamiltonian and initial density matrix, we are interested in the electric current as a time derivative of bath occupation ($\hbar = e = 1$), and the current operator can be evaluated by the following commutator:

$$I_L(t) = -\frac{dN_L(t)}{dt} = -\frac{1}{tr[\rho]} tr\{\rho e^{iHt} i[H, N_L] e^{-iHt}\} \tag{17}$$

$$I_R(t) = \frac{dN_R(t)}{dt} = \frac{1}{tr[\rho]} tr\{\rho e^{iHt} i[H, N_R] e^{-iHt}\} \tag{18}$$

$$I_\xi = i[H, N_\xi] = i \sum_{k_\xi} V_{dk_\xi}(-c_{k_\xi}^+ d + d^+ c_{k_\xi}) \tag{19}$$

In this paper, we evaluate current as the average of left and right currents, and another important physical quantity is the population of the system, following Wang et al.:[10,13]

$$I(t) = \frac{1}{2}[I_L(t) + I_R(t)] = \frac{1}{tr[\rho]} tr\{\rho e^{iHt} I e^{-iHt}\}/2 \tag{20}$$

$$P_d(t) = \frac{1}{tr[\rho]} tr\{\rho e^{iHt} d^+ d e^{-iHt}\} \tag{21}$$

2.2. TD-DMRG Approach. *2.2.1. MPS and MPO.* In order to treat the time-dependent transport problems in a rigorous way, we employ time-dependent density matrix renormalization group (TD-DMRG) algorithms. Below, we will introduce DMRG briefly in the language of matrix product state (MPS) and matrix product operator (MPO) and extend the algorithms to finite temperatures and identical particles.

The wave function is described as a chain product of matrices in the language of MPS:[29,30,48]

$$|\Psi\rangle = \sum_{\{a\},\{\sigma\}} A[1]_{a_1}^{\sigma_1} A[2]_{a_1 a_2}^{\sigma_2} \dots A[n]_{a_{n-1}}^{\sigma_n} |\sigma_1 \sigma_2 \dots \sigma_n\rangle \tag{22}$$

in which a_i denotes the dimension of the ith virtual bond, and σ_i is the physical bond index as shown in Figure 1a.
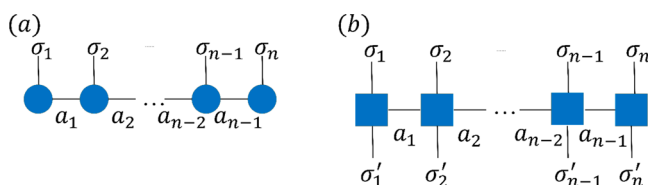

Figure 1. Schematic diagram of (a) MPS and (b) MPO. $\{\sigma, \sigma'\}$ are the physical bonds, and $\{a\}$ is the virtual bonds.

In principle, if the bond dimensions are infinite, then TD-DMRG is able to solve the time-dependent Schrodinger equation exactly. In practice, they have to be truncated. Therefore, extending the virtual bond dimensions can systematically improve the accuracy of the method. The physical bond dimensions denote the basis of each site. Similarly, the operator can be constructed as the following chain of matrices:

$$\hat{O} = \sum_{\{a\},\{\sigma\},\{\sigma'\}} W[1]_{a_1}^{\sigma_1 \sigma_1'} W[2]_{a_1 a_2}^{\sigma_2 \sigma_2'} \dots W[n]_{a_{n-1}}^{\sigma_n \sigma_n'} |\sigma_1 \sigma_2 \dots \sigma_n\rangle$$
$$\langle \sigma_1' \sigma_2' \dots \sigma_n'| \tag{23}$$

in which a_i denotes the dimension of the ith virtual bond, and σ_i and σ_i' are the physical bond indexes as shown in Figure 1b.

2.2.2. Time Evolution Algorithm. To solve the time-dependent Schrodinger equation, we use the time-dependent variational principle (TDVP) method for time evolution. The Dirac−Frenkel TDVP is expressed as

$$\langle \delta\Psi | i \frac{\partial}{\partial t} - \hat{H} | \Psi \rangle = 0 \tag{24}$$

Using the tangent space of $|\Psi(t)\rangle$, the equation can be written as

$$\frac{\partial |\Psi(t)\rangle}{\partial t} = -i\hat{P}\hat{H}|\Psi(t)\rangle \tag{25}$$

$$\hat{P} = \sum_{i=1}^{n} \hat{P}[1: i-1] \otimes \hat{I}_i \otimes \hat{P}[i+1: n]$$
$$- \sum_{i=1}^{n-1} \hat{P}[1: i] \otimes \hat{P}[i+1: n] \tag{26}$$

$\hat{P}$ is the projection operator made up of orthonormal vectors belonging to the tangent space.[32−34] Eq 25 can be regarded as an orthogonal projection onto the current tangent space of $|\Psi(t)\rangle$. Here,

$$\hat{P}[1: i] = \sum_{a_i a_i'} |a_i'[1: i]\rangle \mathbf{S}[1: i]_{a_i' a_i}^{-1} \langle a_i[1: i]| \tag{27}$$

$$\hat{P}[i+1: n] = \sum_{a_i a_i'} |a_i'[i+1: n]\rangle \mathbf{S}[i+1: n]_{a_i' a_i}^{-1} \langle a_i[i+1: n]| \tag{28}$$

$$\hat{I}_i = \sum_{\sigma_i} |\sigma_i\rangle\langle\sigma_i| \tag{29}$$

$$\hat{P}[1: 0] = \hat{P}[n+1: n] = 1 \tag{30}$$

Here, $\mathbf{S}$ is the overlap matrix due to the nonorthogonality of the renormalized basis.[34] Then, after a tiny time Δt propagation, the wave function of eq 25 can be solved as

$$|\Psi(t + \Delta t)\rangle = e^{-i\hat{P}\hat{H}\Delta t}|\Psi(t)\rangle \tag{31}$$

The expectation value of any operator $\hat{F}(t)$ at 0 K is

$$\langle \hat{F}(t) \rangle = \langle \Psi(0)| e^{i\hat{H}t} \hat{F} e^{-i\hat{H}t} |\Psi(0)\rangle \tag{32}$$

in which the time evolution is done as in eq 31, step by step numerically.

2.2.3. Finite Temperature and Imaginary Evolution Algorithm. At a finite temperature, the initial state is not a pure quantum state. It cannot be described by a single MPS. We then apply the thermo field dynamics approach (or "ancilla" or "purification" approach).[30] For any density matrix ρ^P of a quantum system space P we can find a pure state $|PQ\rangle$ in space P and its auxiliary space Q such that $\rho^P = Tr_Q(|PQ\rangle\langle PQ|)$. If ρ^P has orthonormal decomposition, $\sum_i p_i |i^P\rangle\langle i^P|$, then one way to define the pure state is $|PQ\rangle = \sum_i \sqrt{p_i}|i^P\rangle|i^Q\rangle$, which can be easily proved to meet $\rho^P = Tr_Q(|PQ\rangle\langle PQ|)$.

Then, the thermal initial density matrix is

$$\frac{e^{-\beta H}}{Tr(e^{-\beta H})} = \frac{Tr_Q\left(e^{-\beta H/2}\sum_i |i^P\rangle|i^Q\rangle \sum_j \langle j^P|\langle j^Q| e^{-\beta H/2}\right)}{Tr_{PQ}\left(e^{-\beta H/2}\sum_i |i^P\rangle|i^Q\rangle \sum_j \langle j^P|\langle j^Q| e^{-\beta H/2}\right)} \tag{33}$$

So we can define $|\Psi_\beta\rangle_{PQ} = e^{-\beta H/2}\sum_i |i^P\rangle|i^Q\rangle / Z^{1/2}$, which is the imaginary time evolution of $\sum_i |i^P\rangle|i^Q\rangle$), and normalize it at each step. The expectation value of any operator $\hat{F}$ in P space is

$$\frac{Tr(\hat{F}e^{-\beta H})}{Tr(e^{-\beta H})} =$$

$$\frac{Tr_{PQ}\left(\hat{F}e^{-\beta H/2}\sum_i |i^P\rangle|i^Q\rangle \sum_j \langle j^P|\langle j^Q| e^{-\beta H/2}\right)}{Tr_{PQ}\left(e^{-\beta H/2}\sum_i |i^P\rangle|i^Q\rangle \sum_j \langle j^P|\langle j^Q| e^{-\beta H/2}\right)}$$

$$= {}_{PQ}\langle\Psi_\beta|\hat{F}|\Psi_\beta\rangle_{PQ} \tag{34}$$

Actually, the initial thermal density matrix (eq 15) is a grand canonical ensemble (as indicated in Supporting Information 5), which can be obtained by replacing H with $H - \mu N$ in eqs 33 and 34. Since it is diagonal, we can calculate $e^{-\beta(H-\mu N)/2} \sum_i | i^P\rangle |i^Q\rangle / Z^{1/2}$ directly, and there is no need to use TD-DMRG to calculate the imaginary time evolution.

However, we have seen in eq 15 that the initial thermal distribution is the direct product of the system, and all baths and the baths are free fermions and bosons. So, we can use the thermal Bogoliubov transformation.[49] Several articles have already considered the transformation for phonons,[50−52] but not for fermions. The derivation and equations and the results and comparison between the transformation and imaginary time evolution are given in Supporting Information 4.

2.2.4. Jordan-Wigner Transformation. To deal with the many-particle problem for fermions, the antisymmetry property of operators is non-negligible. We employ the Jordan−Wigner transformation to express the Fermion operators into Pauli matrices:

$$
\begin{cases}
a_k^+ = \prod_{l=1}^{k-1} (-\sigma_l^z)\sigma_k^+ \\
a_k^- = \prod_{l=1}^{k-1} (-\sigma_l^z)\sigma_k^-
\end{cases}
\tag{35}
$$

$$
\begin{cases}
a_k^+ a_k^- = \sigma_k^+ \sigma_k^- \\
a_n^+ a_m^- = \sigma_n^+ \prod_{l=n+1}^{m-1} (-\sigma_l^z)\sigma_m^- \ (n < m)
\end{cases}
\tag{36}
$$

Now, the electronic Hamiltonian and the current operator become:

$$
H_{el} = \sum_k E_k c_k^+ c_k + \left(\sum_k V_{dk}\sigma_k^+ \sigma_d^- \prod_{l=\langle k,d\rangle} (-\sigma_l^z) + Hc \right)
\tag{37}
$$

$$
I = \frac{i}{2}\left(\sum_{k_L} V_{dk_L}\sigma_{k_L}^+ \sigma_d^- \prod_{l=\langle k_L,d\rangle} (-\sigma_l^z) - Hc \right)
$$
$$
- \frac{i}{2}\left(\sum_{k_R} V_{dk_R}\sigma_{k_R}^+ \sigma_d^- \prod_{l=\langle k_R,d\rangle} (-\sigma_l^z) - Hc \right)
\tag{38}
$$

in which k can denote the molecular bridge and left and right lead sites, and $\langle k,d\rangle$ means the total product is acquired from all the sites between site k and site d.

2.3. Orbital Ordering and Entanglement Entropy. The orderings of the bath sites (electrons of the leads and phonons) in MPS can make a difference to numerical accuracy.[39,53] Zwolak et al. discussed the purely electronic model and gave a quite reasonable ordering for the star geometry.[39] They ranked the lead electronic sites by energy. Thus, the left and right lead sites could be mixed up. Ranking sites by energy and mixing the left and right lead sites are to localize the entanglement in the bias window and between nearly iso-energetic sites. Different ordering schemes have also been suggested for the chain geometry.[43] However, electron−phonon couplings have not been considered.

In this paper, we extend the appropriate ordering described above to the electron−phonon model. Except for the left and right lead baths, there is a phonon bath. Since they are all only entangled with the system bath, we will not mix the phonon sites and lead electron sites. Therefore, there are only four relative orderings of the phonon sites, and they are given in Figure 2. The white and black circles are lead sites, corresponding to sites above and below the Fermi surface, respectively, i.e., unoccupied and occupied initially. The gray circle is the system site. The blue circles are the phonon sites, and they can be placed on four different relative positions. The relative orderings of the lead sites are kept the same as in ref 39. Since entropy is easy to get in the language of MPS, we will calculate the effective entropy[39] and bond entropy of different orderings and compare and discuss the four orderings in section 3.4.
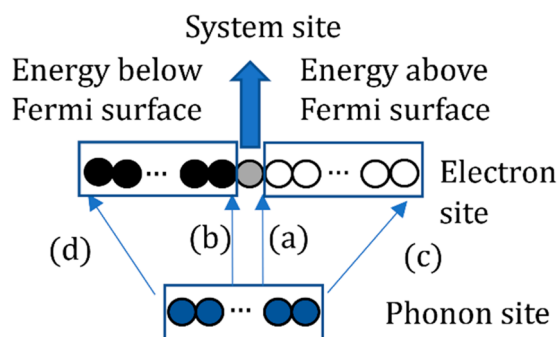

Figure 2. Four orderings of all the sites at 0 K. a and b mean that the phonon sites are placed closely next to the system site, from right or left, respectively. c and d mean that the phonon sites are placed far from the system site. The frames mean that ordering of the phonon or electron sites in the frames is fixed.

3. RESULTS AND DISCUSSION

We employed the TD-DMRG method to investigate the electron transport in a vibrationally coupled molecular junction. The parameters utilized in the model, as detailed in section 2.1, were taken from the literature,[13] $\beta_e = 1$ eV, $\alpha_e = 0.2$ eV, and $\omega_c = 500$ cm^{-1} = 0.062 eV, and remained constant throughout this study. For convergence tests and comparison with ML-MCTDH results,[13] we included the discretization scheme and TD-DMRG parameters in Supporting Information 2. Figure 3 displays the additional parameters we varied to explore vibrationally coupled electron transport at 0 K. One of
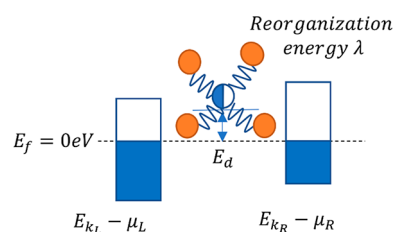

Figure 3. Diagrammatic presentation of the vibrationally coupled molecular junction electron transport at 0 K. The onsite energy E_d of the molecular bridge, initial occupancy of the bridge state, reorganization energy λ, and voltage are tuned to explore the transport. The blue areas are occupied by electrons, and the white areas are empty. The orange circles are phonons.
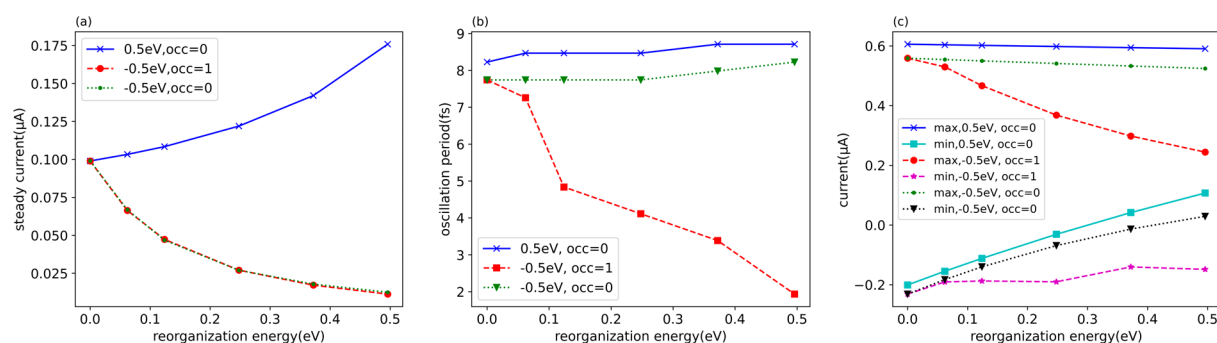
Figure 4. (a) Steady current, (b) oscillation period, and (c) peak value of current versus reorganization energy. The temperature is 0 K. $V = 0.1$ V.
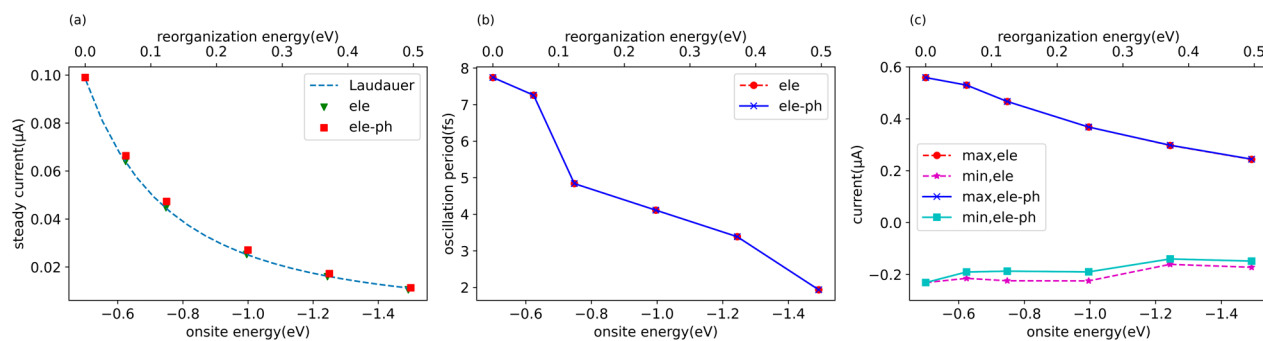

Figure 5. (a) Steady current, (b) oscillation period, and (c) peak value of current versus reorganization energy for the electron phonon model or versus onsite energy for the purely electronic model. The temperature is 0 K. For the electron phonon model, $E_d = -0.5$ eV, and the molecular bridge is initially occupied. $V = 0.1$ V.

these parameters is the on-site energy of the molecular bridge relative to the Fermi surface of the leads, denoted as E_d. Its value can be adjusted using gate voltage.[7,14] Additionally, we set the initial occupancy of the molecular bridge to either zero or one. This choice leads to different phonon initial states and can significantly impact electron transport.[5,46] Another crucial parameter is the strength of electron phonon coupling, determined by α in eq 14 or by the reorganization energy,[46] λ. Last, the voltage or chemical potential of the leads in eq 8 serve as another parameter, for which we provide current–voltage curves in Supporting Information 2. The cases involving finite temperature are discussed in Supporting Information 4.

3.1. Steady Currents, Oscillation Periods, and Peak Values. We then analyze the steady currents, oscillation periods, and peak values of the currents for different reorganization energies. The whole dynamics can be found in Supporting Information 3. We focus our discussion on three initial states: $E_d = 0.5$ eV and initially unoccupied, $E_d = -0.5$ eV and initially occupied, and $E_d = -0.5$ eV and initially unoccupied. In Figure 4a, we observe that for $E_d = 0.5$ eV, the steady current increases as the electron phonon coupling strength rises. Conversely, for $E_d = -0.5$ eV, the opposite trend is observed. Notably, the initial occupancy does not impact the steady current significantly.

In Figure 4b, the oscillation period is determined by examining the highest and lowest peaks of the currents (Supporting Information 3). We observe that, in initially unoccupied cases, the periods remain relatively constant with varying reorganization energy. However, in $E_d = -0.5$ eV and the initially occupied case, the periods decrease as the electron phonon couplings strengthen.

In Figure 4c, we examine the peak value of the currents, which present the oscillation amplitudes. The highest peaks remain unchanged regardless of changes in the reorganization energy in initially unoccupied cases, as depicted in Figure 4b. However, in $E_d = -0.5$ eV and the initially occupied case, the maximum current decreases rapidly with increasing electron phonon couplings. On the other hand, the lowest peaks increase with larger electron phonon couplings in all three cases, resulting in a decay of the oscillation amplitudes. A more detailed analysis and visualization can be found in Supporting Information 3, and we will provide a semiquantitative explanation below.

3.2. Explanation Using Polaron Transformation and Canonical Transformation. The phenomenon in Figure 5a is just like the Marcus formula:[54]

$$k_{\text{Marcus}} = \frac{V^2}{\hbar} \sqrt{\frac{\pi}{\lambda k_B T}} \exp\left[-\frac{(\Delta G + \lambda)}{4\lambda k_B T} \right] \tag{39}$$

in which increasing λ can increase or decrease the rates depending on the sign of ΔG. However, it is important to note that this formula is specifically applicable in the context of organic semiconductors and may not be directly applicable to molecular junctions. Additionally, its effectiveness might be limited when considering the temperature effects.

In the initially unoccupied cases, the observed phenomena can be explained by employing the polaron transformation. For the model in eqs 1–4, it is known that the phonon and system components can be disentangled using a straightforward polaron transformation,[55] disregarding the lead sections:
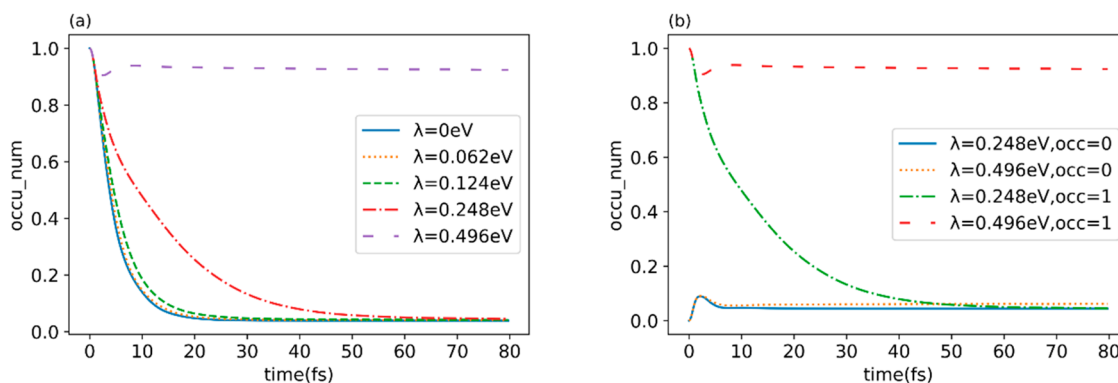
Figure 6. Occupation number of the molecular bridge changes over time (a) for the initially occupied model with different electron−phonon couplings and (b) for the initially occupied and unoccupied model. The other parameters are $T = 0$ K, $E_d = 0.5$ eV, and $V = 0.1$ V.

$$H = E_d d^+ d + \sum_j \omega_j \left(a_j^+ a_j + \frac{1}{2} \right)$$

$$+ \sum_j \frac{c_j}{\sqrt{2\omega_j}} d^+ d (a_j^+ + a_j) \rightarrow H = \left(E_d - \sum_j \frac{c_j^2}{2\omega_j^2} \right) d^+ d$$

$$+ \sum_j \omega_j \left(a_j^+ a_j + \frac{1}{2} \right) \tag{40}$$

Indeed, the electron−phonon coupling has the ability to "lower" the onsite energy of the bridge, and this reduction corresponds to the reorganization energy[46,47] $\lambda = \sum_j c_j^2/(2\omega_j^2)$. This mechanism provides an explanation for the observed changes in steady currents. In the $E_d = 0.5$ eV and initially unoccupied case, where E_d is far above the Fermi surface of the leads, reducing it can enhance the currents. Conversely, in $E_d = -0.5$ eV and initially unoccupied case, where E_d is considerably below the Fermi surface of the leads, reducing it causes the "effective" onsite energy even further away from the Fermi surface. As a result, the steady currents decrease.

In Figure 4b,c, the plots for the initially unoccupied case demonstrate that the electron phonon coupling does not influence the oscillation periods. However, the amplitudes of the oscillations are reduced due to the presence of decoherence. In contrast, the $E_d = -0.5$ eV and initially occupied case exhibits distinct behavior. Changing the initial occupancy significantly alters the oscillation behavior. As mentioned in the following paragraph of eq 15, different initial occupancies lead to distinct H_{nuc}^0 terms. In the case of the initially occupied situation, the phonons do not behave as simple harmonic oscillators before time evolution, but rather as displacement harmonic oscillators:

$$H_{0ph} = \sum_j \omega_j \left(a_j^+ a_j + \frac{1}{2} \right) + \sum_j \frac{c_j}{\sqrt{2\omega_j}} (a_j^+ + a_j) \tag{41}$$

To simplify the model, a canonical transformation[55] can be applied to transform it into a harmonic oscillator model: $a_j = a_j - c_j/(\omega_j \sqrt{2\omega_j})$. This transformation allows for the conversion of the time-evolving Hamiltonian as well:

$$H = E_d d^+ d + \sum_j \omega_j \left(a_j^+ a_j + \frac{1}{2} \right)$$

$$+ \sum_j \frac{c_j}{\sqrt{2\omega_j}} d^+ d (a_j^+ + a_j) \rightarrow H = \left(E_d - \sum_j \frac{c_j^2}{\omega_j^2} \right) d^+ d$$

$$+ \sum_j \omega_j \left(a_j^+ a_j + \frac{1}{2} \right) + \sum_j \frac{c_j}{\sqrt{2\omega_j}} (d^+ d - 1)(a_j^+ + a_j)$$

$$+ \frac{1}{2} \sum_j \frac{c_j^2}{\omega_j^2} \tag{42}$$

The lead parts are omitted since the transformation solely focuses on phonons. Unlike the polaron transformation, this one is exact without any approximations. As a result, the operator representing the electron phonon coupling can be expressed as $\sum_j [c_j/(\sqrt{2\omega_j})](d^+ d - 1)(a_j^+ + a_j)$.

If $d^+ d \approx \langle d^+ d \rangle \approx 1$:

$$H = \left(E_d - \sum_j \frac{c_j^2}{\omega_j^2} \right) d^+ d + \sum_j \omega_j \left(a_j^+ a_j + \frac{1}{2} \right) + \frac{1}{2} \sum_j \frac{c_j^2}{\omega_j^2} \tag{43}$$

The electron and phonon parts are disentangled in this approximation. This "new approximation", as we will refer to it in the subsequent discussions, differs signicantly from the polaron transformation. For the polaron transformation, the phonon operators are replaced by their expectation value. However, in eq 43, the electron operator $d^+ d$ is replaced by its expectation value to eliminate electron phonon coupling. Additionally, it differs from eq 40 in terms of lowering the onsite energy by $\sum_j c_j^2/\omega_j^2 = 2\lambda$ instead of λ.

For the case when $d^+ d \approx 1$, the Hamiltonian described in eq 43 reduces to a purely electronic Hamiltonian. This should yield similar results for the electron phonon model and an "equivalent" purely electronic model, where the steady current can be calculated using the Landauer formula.[11,16,17,56] Figure 5 allows us to verify this assumption. Figure 5a illustrates that the steady currents of the $E_d = -0.5$ eV and initially occupied electron phonon model closely match those of the corresponding purely electronic model and predictions from the Landauer formula. Similarly, Figure 5b,c demonstrate that the oscillation period and peak value of the currents exhibit remarkable similarity between the electron phonon model and corresponding purely electronic model. Thus, the behavior observed in
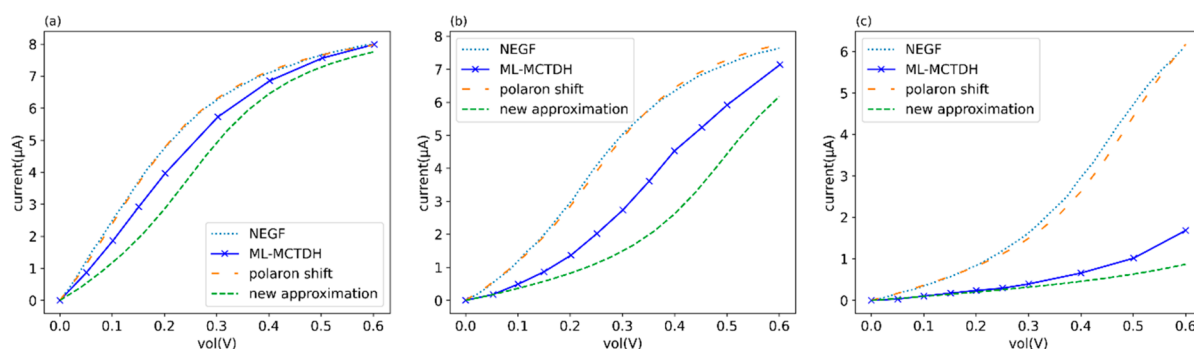
Figure 7. Current−voltage curves of eqs 40 and 43 compared with the results of NEGF and ML-MCTDH for reorganization energy: (a) $\lambda = 0.062$ eV, (b) $\lambda = 0.124$ eV, (c) $\lambda = 0.248$ eV. The other parameters are $T = 0$ K and $E_d = 0$ eV. The ML-MCTDH and NEGF results are from ref 13. Eqs 40 and 43 are combined with the Landauer formula.
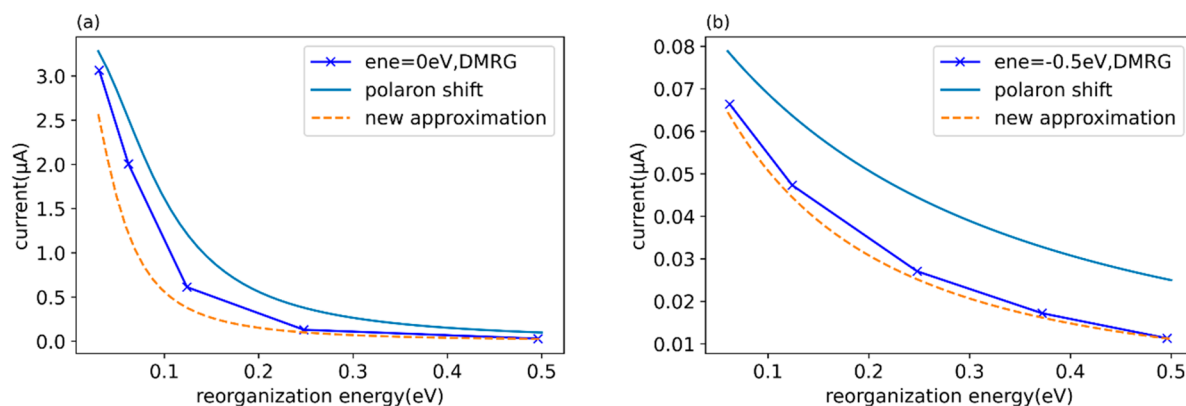

Figure 8. Results of eqs 40 and 43 are compared with the results of DMRG versus reorganization energy with onsite energy (a) $E_d = 0$ eV and (b) $E_d = -0.5$ eV at $T = 0K$.

Figure 4 can be primarily explained as purely electronic behavior rather than as an effect of electron phonon coupling. This comparison further highlights the differences between the polaron transformation and canonical transformation. While they both lower the effective on-site energy and eliminate the electron phonon coupling, the former is primarily used for conceptual understanding and unable to eliminate electron phonon coupling. In contrast, with the latter, the many body effects can be partially eliminated by appropriately selecting the parameters.

It is verified in Figure 5 that the approximation $d^+d \approx 1$ is valid under specific conditions. It is a good approximation when the initial occupancy is unity, and the effective on-site energy is considerably below the Fermi surface. This gives rise to an interesting phenomenon. In $E_d = 0.5$ eV far above the Fermi surface and initially occupied case, different reorganization energies can result in distinct steady occupancies. Figure 6a demonstrates this behavior, showing that for small reorganization energies the occupation number tends to approach zero from unity, while for quite large reorganization energies the occupancy remains close to one. Comparing the $E_d = 0.5$ eV and initially unoccupied case with the initially occupied case, Figure 6b reveals that for small reorganization energies the steady occupancy is independent of the initial occupancy. However, for large reorganization energies, two distinct steady occupancies emerge. This phenomenon is known as bistability.[46] The explanation lies in eqs 40 and 43. In eq 40, the energy is lowered by λ, while in eq 43, the energy is lowered by 2λ. When $\lambda = 0.496$ eV, $E_d - 2\lambda$ is significantly below the Fermi surface, while $E_d - \lambda$ is still above it.

Consequently, distinct steady occupation numbers arise (the "actual" reduction in onsite energy can be a fraction depending on the steady population[57]). For $\lambda = 0.248$ eV, $E_d - 2\lambda$ remains above the Fermi surface, rendering the canonical transformation invalid after a certain time and resulting in the same steady occupancy as the initially unoccupied case. Thus, the polaron transformation and canonical transformation offer a simple criterion for the emergence of bistability.

3.3. Comparison with NEGF. In addition to the bistability phenomenon, the two transformations can be utilized for comparison with the results obtained by the NEGF method. An NEGF approach based on the polaron transformation has been proposed to address electron transport coupled with vibrations.[13,58−60] Figure 7 illustrates the stationary current obtained from the NEGF method alongside the results from eqs 40 and 43, all compared to the ML-MCTDH method, which provides numerically exact results for different electron phonon couplings. The figure shows that the NEGF method is in good agreement with the numerically exact results only for small reorganization energies, where it aligns well with the results obtained from eq 40, as they are both based on polaron transformation. However, eq 40 only considers the polaron shift of the onsite energy, hence we refer to the results from eq 40 as "polaron shift".[13] For larger reorganization energies, the $d^+d \approx 1$ approximation (eq 43) performs significantly better, confirming the validity of our approximation (if we calculate the final occupation number numerically and multiply it with 2λ, the result is even better[57]). When dealing with large electron phonon coupling, simulating the current accurately by using the NEGF method becomes challenging. Nevertheless,
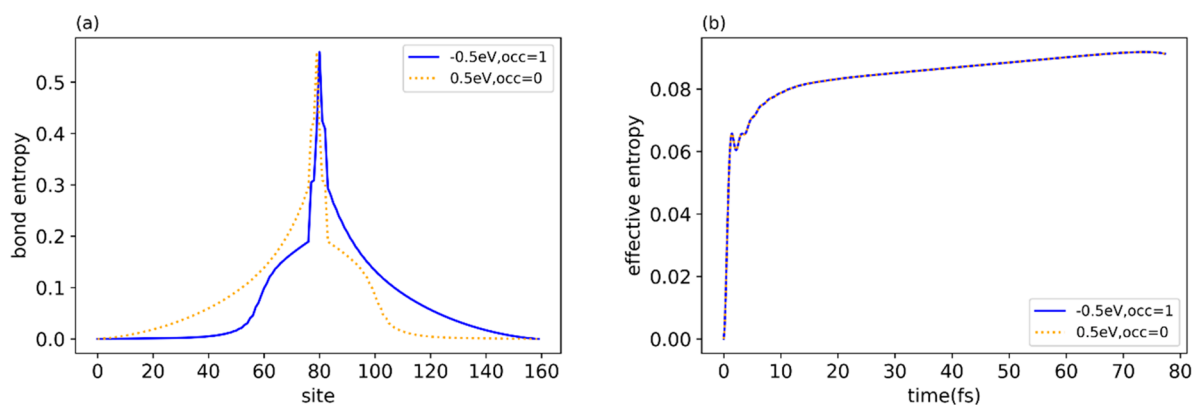
Figure 9. Entropy curves are shown for the purely electronic model. (a) Bond entropy. The peak of the orange line is at site 79 (the initial site number is zero), and the peak of the other is at site 80. (b) Effective entropy at about 77.5 fs. $T = 0$ K, $V = 0.1$ V.
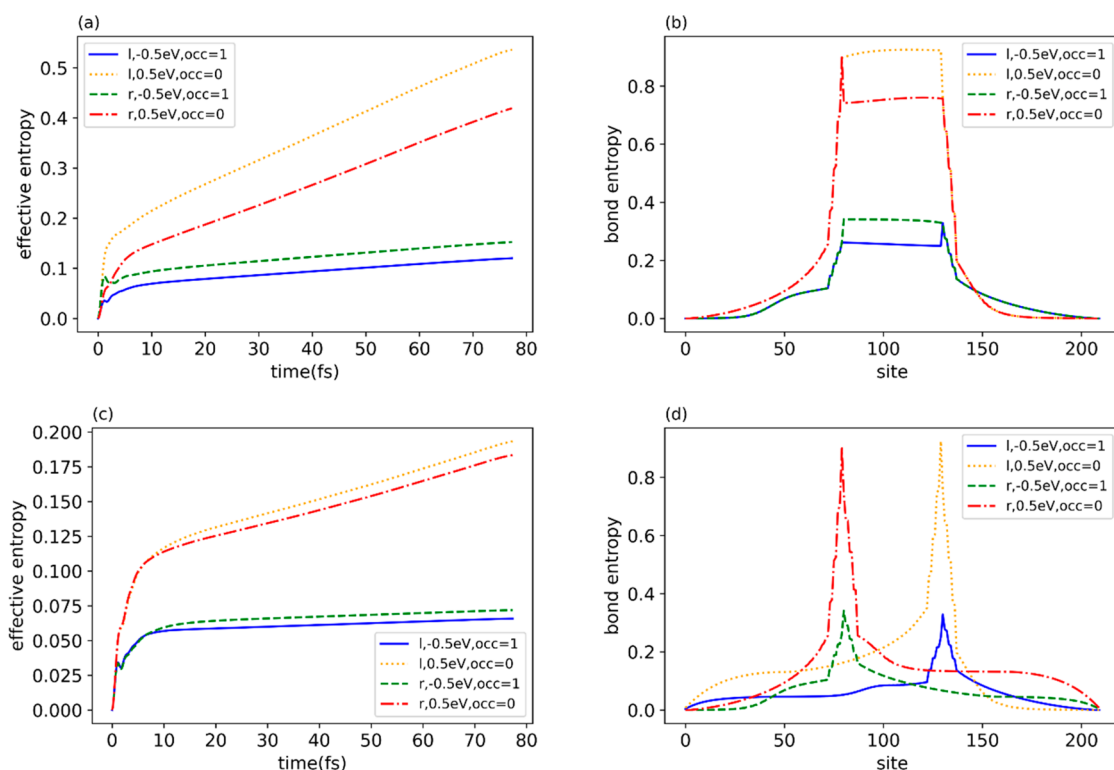

Figure 10. Entropy curves are shown for the electron−phonon model. (a) Effective entropy at about 77.5 fs. (b) Bond entropy of a. c and d are the same as a and b except for the position of the phonon sites. $V = 0.2V$.

for larger reorganization energies, eq 43 provides a closer approximation, consistent with our previous comparisons of the two transformations in different regimes.

In Figure 7, where the on-site energy is set to 0 eV, we observe that for small reorganization energies, the polaron shift approximation in eq 40 provides a valid description. However, for strong electron−phonon couplings, the new approximation in eq 43 outperforms the polaron shift approximation. This is clearly demonstrated in Figure 8a. However, in the $E_d = -0.5$ eV case in Figure 8b, the polaron shift one is not as accurate across all ranges and performs even worse for large reorganization energies. On the other hand, eq 43 exhibits improved accuracy in this scenario. Overall, Figure 8 illustrates that the effective bridge energy differs among the different models used, highlighting the respective scopes of application for the two approximations. Specifically, eq 43 proves to be a

quite reliable approximation in regions where the on-site energy is far below the Fermi surface and in regions with strong electron−phonon couplings. The $E_d = 0.5$ eV case is not discussed due to the presence of bistability phenomena, which significantly influence the steady current as a result of the initial occupation. More detailed information about the time-dependent current can be found in Supporting Information 2.

3.4. Ordering and Entanglement Entropy. In the content of MPS, obtaining the ordering and entanglement entropy is relatively straightforward. The effective entropy can be defined as follows:[39]

$$S_{\mathrm{eff}} = \ln \sqrt[3]{\frac{1}{L-1} \sum_n e^{3S_n}}$$

(44)

In the given equation, L represents the total number of sites, S_n is the entropy for bipartite cuts, and n runs over the entire

MPS chain. Figure 9 represents the effective and bond entropies of the purely electronic model. The system consists of a total of 161 sites (Supporting Information 2). The ordering follows Zwolak's ordering convention,[39] where the lead sites are arranged based on increasing onsite energy, and the single system site is positioned in the middle. As a result, the left half of the system is initially occupied, while the right half remains unoccupied. Figure 9a compares the orange line corresponding to $E_d = 0.5$ eV with an initial occupation of zero and the blue line representing $E_d = -0.5$ eV with an initial occupation of 1. Due to the electron–hole symmetry, these lines should be identical, as verified by Figure 9. It can also be observed that the peak occurs at the interface of the zero Fermi energy. This suggests that the entropy between sites with different occupation numbers or on opposite sides of the Fermi surface is greater than the entropy between sites with similar occupation numbers.[39,43]

In the electron–phonon model, there are 50 phonon modes (Supporting Information 2). In Figure 10a and b, the phonon sites are put on the left or right side of the electronic site within the system, between the lead sites (as shown in Figure 3, labeled as a and b). For the case of $E_d = -0.5$ eV, when the phonon sites are on the left-hand side, the entanglement entropy is smaller; while for the case of $E_d = 0.5$ eV, the ordering with phonon sites on the right-hand site results in smaller entanglement entropy. There is something interesting in Figure 10b, for phonon sites on the left or right of the system site, there is a platform or a peak plus a platform, and the location of the peak is contrary for $E_d = -0.5$ eV versus $E_d = 0.5$ eV.

In Figure 10b, the orange line exhibits a platform from site 79 to site 129, representing the bond entropy between nearest neighbor phonon sites and the bond entropy between terminal phonon sites and either lead sites or the single system site. On the other hand, the red line shows a peak at site 79, located between the single system site and the lead sites, followed by a platform extending from site 80 to site 130, representing bond entropy between nearest neighbor phonon sites and bond entropy between terminal phonon sites and either lead sites or the single system site. This behavior can be understood by considering the combination of maximal entropy across the Fermi surface[39,43] and the polaron transformation. Using the polaron transformation,[13,55] the system site and the phonon sites can be treated as a single entity. In the case of the red line, there is expected to be a large entropy between the almost unoccupied system site and the lead site below the Fermi surface.[39,43] However, the entropy of the phonon site that interacts with the lead site above the Fermi surface should be small. This leads to the observed peak at site 79 and the subsequent platform between the phonon sites shown by the red line. Similarly, for the orange line, the entropy of site 79 is expected to be large due to the same reason, while the entropy of site 130 should be small. Again, there is a platform between phonon sites, resulting in the shape of the orange line. The shapes of the green and blue lines in Figure 10b can also be explained using the same reason, except that the onsite energy is now below the Fermi surface. Consequently, the peak appears at the opposite position.

In Figure 10c and d, the arrangement of phonon sites is the same as in Figure 10a and b, except that the phonon sites are put outside of all the electron sites (as shown in Figure 3, labeled as c and d). Due to this change in placement, there is no longer a high-entropy platform between the phonons,

resulting in smaller effective entropy values, although the largest bond entropy remains the same. For the case of $E_d = 0.5$ eV, when the phonon sites are placed close to the lead sites above the Fermi surface, the entanglement entropy is smaller, as indicated by the red lines in Figure 10c and d. Conversely, for the case of $E_d = -0.5$ eV, the situation is reversed, with a larger entanglement entropy observed for the green lines in Figure 10c and d. When comparing Figure 10b and d, it can be observed that the left part of red and green lines and the right part of orange and blue lines remain the same, respectively.

Based on the analysis of the electron phonon model for a single molecular junction with the given parameters $\beta_e = 1$ eV, $\alpha_e = 0.2$ eV, $\omega_c = 500$ cm^{-1} = 0.062 eV, $\lambda = 0.248$ eV, and $V = 0.2V$, it appears that the optimal ordering is to position the phonon sites outside the electron sites. However, since the entropy values are relatively small compared to the bond dimension (as indicated in Supporting Information 2), the ordering does not significantly impact the time-dependent current.[39] Additionally, it is worth noting that the ordering remains unchanged during time evolution. In future research, the identified orderings can serve as a good initial guess combined with on-the-fly swapping techniques.[61] This approach can be employed to explore the optimal ordering for transport problems involving vibrationally coupled single-molecular junction as well as multimolecular junctions.

4. CONCLUSIONS

In this study, the TD-DMRG algorithms were utilized to investigate the time-dependent current and occupation number of a molecular junction with vibrational coupling. The calculations were performed for both zero- and finite temperature conditions. To gain insights into the behavior of steady currents in the regime of strong electron–phonon coupling, a novel transformation and approximation method was developed.

The proposed TD-DMRG method was extensively tested across a wide range of parameters to demonstrate its correctness and computational feasibility. The results obtained from the method were found to be in excellent agreement with those obtained from ML-MCTDH calculations as well as analytical results obtained in the purely electronic limit.[13,56] This successful comparison validates the accuracy and robustness of the TD-DMRG method for general molecular transport problems involving both electrons and phonons. In the strong electron phonon coupling regime, which is challenging for the NEGF method,[13] our new approximation proves particularly effective. In addition, the study also delves into the entropy of different orderings, expanding the analysis to electron–phonon model problems. These entropy variations are further understood through application of the polaron transformation. Finally, in Supporting Information 4, thermal Bogoliubov transformation of both fermions and bosons is employed to address the finite temperature problems and compared with the results from imaginary time evolution results.

In this paper, the focus was primarily on the charge transport in molecular junctions. Other important aspects are heat transport, thermoelectric properties, and spin currents.[11,12,62,63] As we demonstrated recently, TD-DMRG can be effectively applied to evaluate the thermal electric conversion power factor,[38] and it is expected to explore many thermal effects in molecular junctions, including the Seebeck effect observed in polymeric materials[64,65] and spin Seebeck effect.[17,66] In future

work, we will develop TD-DMRG algorithms for studying transport in molecular junctions. This may involve combining open quantum system methods with MPS[25,67] and going beyond the Lindblad equation[42] to avoid the need for discretizing of the Fermi bath. These advancements will enable more comprehensive investigations into the thermal effects, thermoelectric properties, and spin currents in molecular junctions.

■ ASSOCIATED CONTENT

ⓈⒾ Supporting Information

The Supporting Information is available free of charge at https://pubs.acs.org/doi/10.1021/acs.jctc.3c00340.

> Display of the Poincaré recurrence; convergence tests for the TD-DMRG parameters and comparison with ML-MCTDH; dynamic images of the electron phonon model and purely electronic model; derivation of thermal Bogoliubov transformation of both fermions and bosons at finite temperature; and discussions about the grand canonical ensemble in this model (PDF)

■ AUTHOR INFORMATION

Corresponding Author

Zhigang Shuai − *MOE Key Laboratory of Organic Optoelectronics and Molecular Engineering, Department of Chemistry, Tsinghua University, Beijing 100084, People's Republic of China; School of Science and Engineering, The Chinese University of Hong Kong, Shenzhen, Guangdong 518172, People's Republic of China;* ⓞ orcid.org/0000-0003-3867-2331; Email: zgshuai@tsinghua.edu.cn

Authors

Hengrui Yang − *MOE Key Laboratory of Organic Optoelectronics and Molecular Engineering, Department of Chemistry, Tsinghua University, Beijing 100084, People's Republic of China;* ⓞ orcid.org/0000-0001-8525-9772

Weitang Li − *MOE Key Laboratory of Organic Optoelectronics and Molecular Engineering, Department of Chemistry, Tsinghua University, Beijing 100084, People's Republic of China;* ⓞ orcid.org/0000-0002-8739-641X

Jiajun Ren − *MOE Key Laboratory of Theoretical and Computational Photochemistry, College of Chemistry, Beijing Normal University, Beijing 100875, People's Republic of China;* ⓞ orcid.org/0000-0002-1508-4943

Complete contact information is available at:
https://pubs.acs.org/10.1021/acs.jctc.3c00340

Notes

The authors declare no competing financial interest.

■ ACKNOWLEDGMENTS

■ REFERENCES

(1) Reed, M. A.; Zhou, C.; Muller, C. J.; Burgin, T. P.; Tour, J. M. Conductance of a Molecular Junction. *Science* **1997**, *278* (5336), 252−254.

(2) Nitzan, A.; Ratner, M. A. Electron Transport in Molecular Wire Junctions. *Science* **2003**, *300* (5624), 1384−1389.

(3) Joachim, C.; Gimzewski, J. K.; Aviram, A. Electronics Using Hybrid-Molecular and Mono-Molecular Devices. *Nature* **2000**, *408* (6812), 541−548.

(4) Chen, F.; Hihath, J.; Huang, Z.; Li, X.; Tao, N. J. Measurement of Single-Molecule Conductance. *Annu. Rev. Phys. Chem.* **2007**, *58* (1), 535−564.

(5) Galperin, M.; Ratner, M. A.; Nitzan, A.; Troisi, A. Nuclear Coupling and Polarization in Molecular Transport Junctions: Beyond Tunneling to Function. *Science* **2008**, *319* (5866), 1056−1060.

(6) Nitzan, A. Electron Transmission through Molecules and Molecular Interfaces. *Annu. Rev. Phys. Chem.* **2001**, *52* (1), 681−750.

(7) Selzer, Y.; Allara, D. L. Single-Molecule Electrical Junctions. *Annu. Rev. Phys. Chem.* **2006**, *57* (1), 593−623.

(8) Liang, W.; Shores, M. P.; Bockrath, M.; Long, J. R.; Park, H. Kondo Resonance in a Single-Molecule Transistor. *Nature* **2002**, *417* (6890), 725−729.

(9) Choi, B.-Y.; Kahng, S.-J.; Kim, S.; Kim, H.; Kim, H. W.; Song, Y. J.; Ihm, J.; Kuk, Y. Conformational Molecular Switch of the Azobenzene Molecule: A Scanning Tunneling Microscopy Study. *Phys. Rev. Lett.* **2006**, *96* (15), No. 156106.

(10) Wang, H.; Thoss, M. Numerically Exact, Time-Dependent Study of Correlated Electron Transport in Model Molecular Junctions. *J. Chem. Phys.* **2013**, *138* (13), No. 134704.

(11) Guo, A.-M.; Sun, Q. Spin-Selective Transport of Electrons in DNA Double Helix. *Phys. Rev. Lett.* **2012**, *108* (21), No. 218102.

(12) Göhler, B.; Hamelbeck, V.; Markus, T. Z.; Kettner, M.; Hanne, G. F.; Vager, Z.; Naaman, R.; Zacharias, H. Spin Selectivity in Electron Transmission Through Self-Assembled Monolayers of Double-Stranded DNA. *Science* **2011**, *331* (6019), 894−897.

(13) Wang, H.; Pshenichnyuk, I.; Härtle, R.; Thoss, M. Numerically Exact, Time-Dependent Treatment of Vibrationally Coupled Electron Transport in Single-Molecule Junctions. *J. Chem. Phys.* **2011**, *135* (24), No. 244506.

(14) Park, H.; Park, J.; Lim, A. K. L.; Anderson, E. H.; Alivisatos, A. P.; McEuen, P. L. Nanomechanical Oscillations in a Single-C60 Transistor. *Nature* **2000**, *407* (6800), 57−60.

(15) Wang, L.; Nan, G.; Yang, X.; Peng, Q.; Li, Q.; Shuai, Z. Computational Methods for Design of Organic Materials with High Charge Mobility. *Chem. Soc. Rev.* **2010**, *39* (2), 423−434.

(16) Golizadeh-Mojarad, R.; Datta, S. Nonequilibrium Green's Function Based Models for Dephasing in Quantum Transport. *Phys. Rev. B* **2007**, *75* (8), No. 081301.

(17) Xiao-Bin, C.; Wen-Hui, D. Quantum Thermal Transport and Spin Thermoelectrics in Low-Dimensional Nano Systems: Application of Nonequilibrium Green's Function Method. *Acta Physica Sinica* **2015**, *64*, No. 186302.

(18) Mitra, A.; Aleiner, I.; Millis, A. J. Phonon Effects in Molecular Transistors: Quantal and Classical Treatment. *Phys. Rev. B* **2004**, *69* (24), No. 245302.

(19) Benesch, C.; Čížek, M.; Klimeš, J.; Kondov, I.; Thoss, M.; Domcke, W. Vibronic Effects in Single Molecule Conductance: First-Principles Description and Application to Benzenealkanethiolates between Gold Electrodes. *J. Phys. Chem. C* **2008**, *112* (26), 9880−9890.

(20) Sowa, J. K.; Mol, J. A.; Briggs, G. A. D.; Gauger, E. M. Beyond Marcus Theory and the Landauer-Büttiker Approach in Molecular Junctions: A Unified Framework. *J. Chem. Phys.* **2018**, *149* (15), No. 154112.

(21) Dzhioev, A. A.; Kosov, D. S. Super-Fermion Representation of Quantum Kinetic Equations for the Electron Transport Problem. *J. Chem. Phys.* **2011**, *134* (4), No. 044121.

(22) Werner, P.; Oka, T.; Millis, A. J. Diagrammatic Monte Carlo Simulation of Nonequilibrium Systems. *Phys. Rev. B* **2009**, *79* (3), No. 035320.

(23) Wolf, F. A.; McCulloch, I. P.; Schollwöck, U. Solving Nonequilibrium Dynamical Mean-Field Theory Using Matrix Product States. *Phys. Rev. B* **2014**, *90* (23), No. 235131.

(24) Anders, F. B. Steady-State Currents through Nanodevices: A Scattering-States Numerical Renormalization-Group Approach to Open Quantum Systems. *Phys. Rev. Lett.* **2008**, *101* (6), No. 066804.

(25) Ke, Y.; Borrelli, R.; Thoss, M. Hierarchical Equations of Motion Approach to Hybrid Fermionic and Bosonic Environments: Matrix Product State Formulation in Twin Space. *J. Chem. Phys.* **2022**, *156* (19), No. 194102.

(26) Orús, R. Tensor Networks for Complex Quantum Systems. *Nat. Rev. Phys.* **2019**, *1* (9), 538−550.

(27) White, S. R. Density Matrix Formulation for Quantum Renormalization Groups. *Phys. Rev. Lett.* **1992**, *69* (19), 2863−2866.

(28) White, S. R. Density-Matrix Algorithms for Quantum Renormalization Groups. *Phys. Rev. B* **1993**, *48* (14), 10345−10356.

(29) Jiang, T.; Li, W.; Ren, J.; Shuai, Z. Finite Temperature Dynamical Density Matrix Renormalization Group for Spectroscopy in Frequency Domain. *J. Phys. Chem. Lett.* **2020**, *11* (10), 3761−3768.

(30) Ren, J.; Shuai, Z.; Kin-Lic Chan, G. Time-Dependent Density Matrix Renormalization Group Algorithms for Nearly Exact Absorption and Fluorescence Spectra of Molecular Aggregates at Both Zero and Finite Temperature. *J. Chem. Theory Comput.* **2018**, *14* (10), 5027−5039.

(31) Schollwöck, U. The Density-Matrix Renormalization Group in the Age of Matrix Product States. *Ann. Phys.* **2011**, *326* (1), 96−192.

(32) Haegeman, J.; Cirac, J. I.; Osborne, T. J.; Pizorn, I.; Verschelde, H.; Verstraete, F. Time-Dependent Variational Principle for Quantum Lattices. *Phys. Rev. Lett.* **2011**, *107* (7), No. 070601.

(33) Haegeman, J.; Lubich, C.; Oseledets, I.; Vandereycken, B.; Verstraete, F. Unifying Time Evolution and Optimization with Matrix Product States. *Phys. Rev. B* **2016**, *94* (16), No. 165116.

(34) Li, W.; Ren, J.; Shuai, Z. Numerical Assessment for Accuracy and GPU Acceleration of TD-DMRG Time Evolution Schemes. *J. Chem. Phys.* **2020**, *152* (2), No. 024127.

(35) Ren, J.; Li, W.; Jiang, T.; Shuai, Z. A General Automatic Method for Optimal Construction of Matrix Product Operators Using Bipartite Graph Theory. *J. Chem. Phys.* **2020**, *153* (8), No. 084118.

(36) Li, W.; Ren, J.; Shuai, Z. Finite-Temperature TD-DMRG for the Carrier Mobility of Organic Semiconductors. *J. Phys. Chem. Lett.* **2020**, *11* (13), 4930−4936.

(37) Li, W.; Ren, J.; Shuai, Z. A General Charge Transport Picture for Organic Semiconductors with Nonlocal Electron-Phonon Couplings. *Nat. Commun.* **2021**, *12* (1), 4260.

(38) Ge, Y.; Li, W.; Ren, J.; Shuai, Z. Computational Method for Evaluating the Thermoelectric Power Factor for Organic Materials Modeled by the Holstein Model: A Time-Dependent Density Matrix Renormalization Group Formalism. *J. Chem. Theory Comput.* **2022**, *18* (11), 6437−6446.

(39) Rams, M. M.; Zwolak, M. Breaking the Entanglement Barrier: Tensor Network Simulation of Quantum Transport. *Phys. Rev. Lett.* **2020**, *124* (13), No. 137701.

(40) Wójtowicz, G.; Elenewski, J. E.; Rams, M. M.; Zwolak, M. Open-System Tensor Networks and Kramers' Crossover for Quantum Transport. *Phys. Rev. A* **2020**, *101* (5), No. 050301.

(41) Chung, C.-M.; Wauters, M. M.; Burrello, M. Matrix Product State Simulations of Quantum Quenches and Transport in Coulomb Blockaded Superconducting Devices. *arXiv* **2022**, DOI: 10.48550/ARXIV.2207.00948.

(42) Brenes, M.; Mendoza-Arenas, J. J.; Purkayastha, A.; Mitchison, M. T.; Clark, S. R.; Goold, J. Tensor-Network Method to Simulate Strongly Interacting Quantum Thermal Machines. *Phys. Rev. X* **2020**, *10* (3), No. 031040.

(43) Kohn, L.; Santoro, G. E. Efficient Mapping for Anderson Impurity Problems with Matrix Product States. *Phys. Rev. B* **2021**, *104* (1), No. 014303.

(44) Nüßeler, A.; Dhand, I.; Huelga, S. F.; Plenio, M. B. Efficient Simulation of Open Quantum Systems Coupled to a Fermionic Bath. *Phys. Rev. B* **2020**, *101* (15), No. 155134.

(45) Elenewski, J. E.; Wójtowicz, G.; Rams, M. M.; Zwolak, M. Performance of Reservoir Discretizations in Quantum Transport Simulations. *J. Chem. Phys.* **2021**, *155* (12), No. 124117.

(46) Wilner, E. Y.; Wang, H.; Cohen, G.; Thoss, M.; Rabani, E. Bistability in a Nonequilibrium Quantum System with Electron-Phonon Interactions. *Phys. Rev. B* **2013**, *88* (4), No. 045137.

(47) Albrecht, K. F.; Wang, H.; Mühlbacher, L.; Thoss, M.; Komnik, A. Bistability Signatures in Nonequilibrium Charge Transport through Molecular Quantum Dots. *Phys. Rev. B* **2012**, *86* (8), No. 081412.

(48) Chan, G. K.-L.; Keselman, A.; Nakatani, N.; Li, Z.; White, S. R. Matrix Product Operators, Matrix Product States, and Ab Initio Density Matrix Renormalization Group Algorithms. *J. Chem. Phys.* **2016**, *145* (1), No. 014102.

(49) TAKAHASHI, Y.; UMEZAWA, H. THERMO FIELD DYNAMICS. *Int. J. Mod. Phys. B* **1996**, *10* (13n14), 1755−1805.

(50) Fischer, E. W.; Saalfrank, P. A Thermofield-Based Multilayer Multiconfigurational Time-Dependent Hartree Approach to Non-Adiabatic Quantum Dynamics at Finite Temperature. *J. Chem. Phys.* **2021**, *155* (13), No. 134109.

(51) Lyu, N.; Mulvihill, E.; Soley, M. B.; Geva, E.; Batista, V. S. Tensor-Train Thermo-Field Memory Kernels for Generalized Quantum Master Equations. *arXiv* **2022**, DOI: 10.48550/arXiv.2208.14273.

(52) Ren, J.; Li, W.; Jiang, T.; Wang, Y.; Shuai, Z. Time-Dependent Density Matrix Renormalization Group Method for Quantum Dynamics in Complex Systems. *WIREs Comput. Mol. Sci.* **2022**, *12* (6), No. e1614.

(53) He, Z.; Millis, A. J. Entanglement Entropy and Computational Complexity of the Anderson Impurity Model out of Equilibrium: Quench Dynamics. *Phys. Rev. B* **2017**, *96* (8), No. 085107.

(54) Shuai, Z.; Li, W.; Ren, J.; Jiang, Y.; Geng, H. Applying Marcus Theory to Describe the Carrier Transports in Organic Semi-conductors: Limitations and Beyond. *J. Chem. Phys.* **2020**, *153* (8), No. 080902.

(55) Mahan, G. *Many-Particle Physics*; Springer: Boston, 2000.

(56) Datta, S. *Electronic Transport in Mesoscopic Systems*; Cambridge Studies in Semiconductor Physics and Microelectronic Engineering; Cambridge University Press: Cambridge, 1995. DOI: 10.1017/CBO9780511805776.

(57) Wang, H.; Thoss, M. Employing an Interaction Picture to Remove Artificial Correlations in Multilayer Multiconfiguration Time-Dependent Hartree Simulations. *J. Chem. Phys.* **2016**, *145* (16), No. 164105.

(58) Galperin, M.; Nitzan, A.; Ratner, M. A. Resonant Inelastic Tunneling in Molecular Junctions. *Phys. Rev. B* **2006**, *73* (4), No. 045314.

(59) Härtle, R.; Benesch, C.; Thoss, M. Multimode Vibrational Effects in Single-Molecule Conductance: A Nonequilibrium Green's Function Approach. *Phys. Rev. B* **2008**, *77* (20), No. 205314.

(60) Härtle, R.; Benesch, C.; Thoss, M. Vibrational Nonequilibrium Effects in the Conductance of Single Molecules with Multiple Electronic States. *Phys. Rev. Lett.* **2009**, *102* (14), No. 146801.

(61) Li, W.; Ren, J.; Yang, H.; Shuai, Z. On the Fly Swapping Algorithm for Ordering of Degrees of Freedom in Density Matrix Renormalization Group. *J. Phys.: Condens. Matter* **2022**, *34* (25), No. 254003.

(62) Thoss, M.; Evers, F. Perspective: Theory of Quantum Transport in Molecular Junctions. *J. Chem. Phys.* **2018**, *148* (3), No. 030901.

(63) Fransson, J. Charge Redistribution and Spin Polarization Driven by Correlation Induced Electron Exchange in Chiral Molecules. *Nano Lett.* **2021**, *21* (7), 3026−3032.

(64) Ge, Y.; Liu, R.; Shuai, Z. Abnormal Seebeck Effect in Doped Conducting Polymers. *Appl. Phys. Lett.* **2021**, *118* (12), No. 123301.

(65) Liu, R.; Ge, Y.; Wang, D.; Shuai, Z. Understanding the Temperature Dependence of the Seebeck Coefficient from First-

Principles Band Structure Calculations for Organic Thermoelectric Materials. *CCS Chem.* **2021**, 3 (10), 1477−1483.

(66) Kim, K.; Vetter, E.; Yan, L.; Yang, C.; Wang, Z.; Sun, R.; Yang, Y.; Comstock, A. H.; Li, X.; Zhou, J.; Zhang, L.; You, W.; Sun, D.; Liu, J. Chiral-Phonon-Activated Spin Seebeck Effect. *Nat. Mater.* **2023**, 22 (3), 322−328.

(67) Gao, X.; Ren, J.; Eisfeld, A.; Shuai, Z. Non-Markovian Stochastic Schrödinger Equation: Matrix-Product-State Approach to the Hierarchy of Pure States. *Phys. Rev. A* **2022**, 105 (3), No. L030202.

📖 **Recommended by ACS**

Molecular Control of Floquet Topological Phase in Non-adiabatic Thouless Pumping

Ruiyi Zhou and Yosuke Kanai

SEPTEMBER 06, 2023
THE JOURNAL OF PHYSICAL CHEMISTRY LETTERS

READ ☑

Modified Ziman Resistivity Formula Valid for the Case of the Fermi Level Near a Band Edge

Shuo Zhao, Yisong Zheng, *et al.*

JULY 11, 2023
THE JOURNAL OF PHYSICAL CHEMISTRY C

READ ☑

Nonempirical Range-Separated Hybrid Functional with Spatially Dependent Screened Exchange

Jiawei Zhan, Giulia Galli, *et al.*

AUGUST 17, 2023
JOURNAL OF CHEMICAL THEORY AND COMPUTATION

READ ☑

New Methodology to Produce Sets of Valence Bond Structures with Enhanced Chemical Insights

Sourav Roy and Avital Shurki

MAY 15, 2023
JOURNAL OF CHEMICAL THEORY AND COMPUTATION

READ ☑

Get More Suggestions >